JOURNAL OF AIRCRAFT
Vol. 48, No. 2, March–April 2011

# Flight Dynamics and Stability of a Tethered Inflatable Kiteplane

E. J. Terink,* J. Breukels,† R. Schmehl,‡ and W. J. Ockels§
*Delft University of Technology, 2629 HS Delft, The Netherlands*

DOI: 10.2514/1.C031108

**The combination of lightweight flexible-membrane design and favorable control characteristics renders tethered inflatable airplanes an attractive option for high-altitude wind power systems. This paper presents an analysis of the flight dynamics and stability of such a kiteplane operated on a single-line tether with a two-line bridle. The equations of motion of the rigid-body model are derived by Lagrange's equation, which implicitly accounts for the kinematic constraints due to the bridle. The tether and bridle are approximated by straight line elements. The aerodynamic force distribution is represented by four discrete force vectors according to the major structural elements of the kiteplane. A case study comprising analytical analysis and numerical simulation reveals that the amount and distribution of lateral aerodynamic surface area is decisive for flight dynamic stability for the specific kite design investigated. Depending on the combination of wing dihedral angle and vertical tail plane size, the pendulum motion shows either diverging oscillation, stable oscillation, converging oscillation, aperiodic convergence, or aperiodic divergence. It is concluded that dynamical stability requires a small vertical tail plane and a large dihedral angle to allow for sufficient sideslip and a strong sideslip response.**

## Nomenclature

| | | |
|---|---|---|
| $A$ | = | aspect ratio |
| $C_D$ | = | aerodynamic drag coefficient |
| $C_L$ | = | aerodynamic lift coefficient |
| $C_{m_{\mathrm{ac}}}$ | = | pitch moment coefficient |
| $\bar{c}$ | = | mean aerodynamic chord, m |
| $D$ | = | aerodynamic drag, N |
| $d$ | = | tether damping constant, Ns/m |
| $\mathbf{F}_a$ | = | aerodynamic force vector, N |
| $F_B$ | = | bridle force, N |
| $\mathbf{F}_{\mathrm{GS}}$ | = | ground-station force vector, N |
| $F_Z$ | = | gravitational force, N |
| $\mathbf{g}$ | = | gravitational acceleration vector, m/s$^2$ |
| $\mathbb{I}$ | = | inertia matrix, kgm$^2$ |
| $k$ | = | tether spring constant, N/m |
| $L$ | = | aerodynamic lift, N |
| $l$ | = | length, m |
| $\mathbf{M}_a$ | = | aerodynamic moment vector, Nm |
| $M_{w_{\mathrm{ac}}}$ | = | wing pitching moment, Nm |
| $m_g$ | = | kite mass excluding confined air, kg |
| $m_k$ | = | kite mass, kg |
| $Q$ | = | generalized force, N |
| $q$ | = | generalized coordinate |
| $\mathbf{r}$ | = | position vector, m |
| $S$ | = | surface area, m$^2$ |
| $T$ | = | kinetic energy, J |
| $\mathbb{T}_{BA}$ | = | transformation matrix for frame A to B |
| $V$ | = | potential energy, J |
| $v$ | = | velocity, m/s |
| $\mathbf{v}$ | = | velocity vector, m/s |
| $X$ | = | aerodynamic force in $X$ direction, N |
| $X, Y, Z$ | = | Cartesian axis system |
| $x, y, z$ | = | Cartesian coordinates, m |
| $Y$ | = | aerodynamic force in $Y$ direction, N |
| $\bar{y}$ | = | spanwise location of mean aerodynamic chord, m |
| $\alpha$ | = | angle of attack, deg |
| $\beta$ | = | sideslip angle, deg |
| $\Gamma$ | = | dihedral angle, deg |
| $\delta$ | = | bridle geometry angle, deg |
| $\theta$ | = | pitch angle, deg |
| $\theta_T$ | = | pendulum mode angle, deg |
| $\Lambda$ | = | sweep angle, deg |
| $\lambda$ | = | wing taper ratio |
| $\rho$ | = | air density, kg/m$^3$ |
| $\phi$ | = | zenith angle, deg |
| $\chi$ | = | bridle angle, deg |
| $\psi$ | = | azimuth angle, deg |
| $\boldsymbol{\omega}$ | = | angular velocity vector, rad/s |

*Subscripts*

| | | |
|---|---|---|
| app | = | apparent |
| c.g. | = | center of gravity |
| $f$ | = | vertical tail fin |
| HT | = | horizontal tail |
| LE | = | leading edge |
| lw | = | left wing |
| rw | = | right wing |
| $T$ | = | tether |
| $t$ | = | tail |
| VT | = | vertical tail |
| $W$ | = | wind |
| $w$ | = | wing |

*Superscripts*

| | | |
|---|---|---|
| $a$ | = | aerodynamic reference frame |
| $B$ | = | body reference frame |
| $E$ | = | Earth reference frame |
| $T$ | = | tether reference frame |

Received 20 May 2010; revision received 9 October 2010; accepted for publication 7 November 2010. 

*Researcher, Institute for Applied Sustainable Science Engineering and Technology, Kluyverweg 1.

†Ph.D. Candidate, Applied Sustainable Science Engineering and Technology Institute, Kluyverweg 1.

‡Associate Professor, Institute for Applied Sustainable Science Engineering and Technology, Kluyverweg 1.

§Professor, Chair Holder, and Director, Institute for Applied Sustainable Science Engineering and Technology, Kluyverweg 1.

## I. Introduction

KITES are among the earliest man-made flying objects in history and have been used for a wide variety of purposes [1]. Especially from 1860 to 1910, kites emerged as an important

technology for scientific and technical applications such as in meteorology, aeronautics, wireless communication, and aerial photography. Although the airplane has subsequently taken over these application areas, kites have made a comeback as major recreational devices. The increasing shift toward sustainable energy generation and propulsion has triggered a renewed interest in kites for industrial applications, and a major driver is the potential of the technology to efficiently exploit the abundant wind at higher altitudes [2,3]. Using kites for power generation was first proposed and systematically analyzed by Loyd in 1980 [4]; however, subsequent research and development activities were rare before the presentation of the laddermill concept by Ockels in 1996 [5,6]. Since then, the number of institutions actively involved in kite power has increased rapidly, including several multimillion-dollar projects [7,8].

Various concepts and ideas have been proposed to exploit the wind currents at higher altitudes [8,9]. One of the concepts is the pumping-kite concept [10,11], where the tether, pulled by lifting bodies, drives a drum that is connected to a generator to produce electricity. By alternating between a high-power-producing upstroke and a low-power-consuming downstroke, net energy is generated. The main advantages of such a system over conventional wind turbines are the higher operational flexibility and the ability to exploit the stronger and steadier wind at higher altitudes. However, the high degree of freedom in the design and operation of kite power systems also leads to control challenges. Compared with an airplane, the flight dynamics of a kite are constrained by the tether and bridle system. However, this does not mean that kites are more stable and easier to control. Research indicates that the presence of a tether may raise stability issues [12–14].

A successful pumping-kite power system requires a kite that is not only agile and aerodynamically efficient to maximize the power output, but that is also stable, to minimize the control effort. In addition, a low-lift mode (in kite terminology, called depower) is necessary to implement a swift low-power-consuming downstroke. Some kite types are naturally stable on a single line (such as box kites, sled kites, delta kites, and some ram-air kites), but none meets the full set of requirements. The kiteplane depicted in Fig. 1, has been developed at the Institute for Applied Sustainable Science Engineering and Technology of Delft University of Technology to operate in a pumping-kite concept [15–17]. The airplane-shaped kite is constructed from inflatable beams and canopy surfaces. It features a bridled wing, efficient aerodynamics for a kite, and easy angle-of-attack control. However, flight tests have indicated that the prototype of 2009 suffers from a pendulum instability, which is an unstable oscillation in the crosswind plane.

In an early scientific contribution, Bryant et al. [12] proposed equations of motion for kites and towed gliders. However, the basic empirical cable model becomes singular when approaching a straight line. Glauert [18] investigated the stability of towed bodies behind an aircraft and provided insight into tether interaction, and Jackson [19] analyzed kites in a large 24 ft wind tunnel. Sanchez [20] started from Lagrangian equations of motion to formulate a model for longitudinal dynamics of a kite and used this to develop a controller for the symmetric flight mode. Alexander and Stevenson [21] dealt with the existence of possible static equilibrium points, and Jackson [22] investigated the shape of the kite in relation to its optimal loading using a static analysis based on Prandtl's lifting-line theory.

**Fig. 1 Photograph of the kiteplane in flight.**

This paper presents a rigid-body model of a single-line bridled kiteplane to investigate the influence of geometry on flight dynamics and stability. The bridle is used not only as a structural element to alleviate the wing bending moment, but it also constrains the rotational freedom of the kite. The roll and yaw motions of the kite are coupled, because the bridle acts as a revolute joint between the tether and the kiteplane. At a high elevation angle, the roll motion is constrained, and at a low elevation angle, the yaw motion is constrained. At intermediate angles, the motion is a combination of roll and yaw. The continuous aerodynamic load distribution is represented by discrete forces and moments acting on the aerodynamically active structural elements of the kiteplane to make the model largely parametric in geometry. The kite system model is described in the Methodology section and applies to kites that are built out of planar aerodynamic elements and for which global geometry and inertia can be assumed constant.

The developed model is subsequently employed to analyze the stability of the kiteplane in a case study. Both analytical and numerical results are obtained and compared qualitatively with each other and with a flight test. Stable and unstable domains are identified and tested on robustness by varying geometry and operational conditions in the simulations.

## II. Methodology

This paper focuses on the influence of geometrical design parameters on the global dynamics of a single-line kite system. Several modeling methods are found in Williams et al. [23]. Optimal control problems for kite systems are often solved using point-mass models [24–26]. Kite performance is investigated using lumped-mass and massless models [27]. For stability, however, attitude dynamics are essential and a point-mass model cannot be used. Also, a flexible-body model would not provide pure geometry-stability relations. Given this scope and the philosophy that the best model is the smallest model that describes the behavior of interest, a rigid-body approach is selected to model the kite.

Moreover, to investigate the impact of geometry changes on stability, a parametric approach is required for the aerodynamic forces. To this end, strip theory is used for the aerodynamic element discretization, similar to the approach used by Meijaard et al. [28]. Strip theory is especially popular in flapping-wing modeling [29,30].

The equations of motion are derived using Lagrange's equation of the second kind [31], a method used frequently for the constrained kite systems [32–34].

### A. Kite System Definition

The kite system consists of a ground station, tether, bridle, and kite. The ground station is represented as a point acting as a forced sink and source of tether length. Tether and bridle are modeled as a single massless rigid body that is free to rotate about the longitudinal axis of the tether. In this idealized system, the tether is connected to the ground station by a spherical and a translational joint. The kite is represented as a rigid body and connected to the bridle by a revolute joint. The five degrees of freedom (DOF) of this system are illustrated in Figs. 2 and 3.

The rotation around the spherical joint is described by the azimuth angle $\psi$, the zenith angle $\phi$, and the bridle rotation angle $\chi$. The translation along the tether longitudinal axis is described by the tether length $l_T$, and the rotation of the kite around the axis connecting the two bridle attachment points (the dashed line in Fig. 3) is described by the pitch rotation angle $\theta$.

The bridle constrains the freedom of the kite with respect to the tether and couples the roll and yaw motions, as explained in the Introduction. The orientation of the bridle with respect to the tether is assumed to be invariant, although, in theory, this specific geometry will allow for some rolling motion. This motion is neglected, because 1) such asymmetric flight conditions are not sustained and the inertia for this motion is low and 2) this motion has not been observed in flight tests.

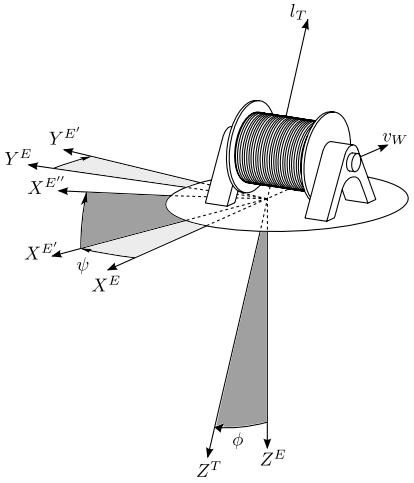


**Fig. 2 Definition of azimuth angle $\psi$ and zenith angle $\phi$.**

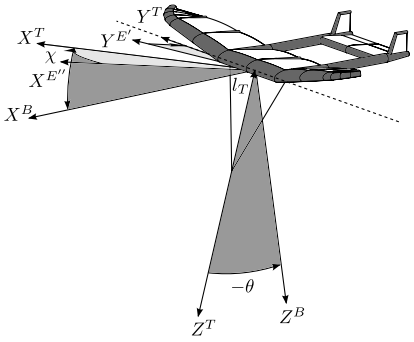


**Fig. 3 Definition of bridle rotation angle $\chi$ and pitch rotation angle $\theta$.**

The assumption of a straight, dragless, and massless tether is valid only for sufficiently short tethers. The tether used for high-altitude wind power systems is generally made from fibers with a high specific tensile strength, such as Dyneema®. Because of this, the diameter of the cable is only a few millimeters, resulting in low mass and small cross-sectional area exposed to the wind. Numerical simulations of a tether discretized by multiple connected rigid elements have shown that for sufficiently large kites and short tether length (shorter than 100 m), the sag in the cable is negligible [35]. The tension in the tether is far greater than the aerodynamic drag forces. For longer tethers, this assumption does not hold; however, for the configurations discussed in this paper, this was not the case. Moreover, the motion constraints in the model lose validity if the tether tension drops to zero, but in the simulations it was verified that this did not occur.

The kite system definitions use the inertial Earth reference frame, a tether reference frame, a body reference frame, and an aerodynamic reference frame. As depicted in Fig. 2, the $-X^E$ axis coincides with the wind vector $v_W$. The azimuth and zenith angles are the result of subsequent rotation about $Z^E$ and $Y^{E'}$, such that $-Z^T$ coincides with the direction of the tether.

With the definition that the origin of the body reference frame coincides with the center of gravity (c.g.), the location of the c.g. in the Earth reference frame can be expressed as

$$\mathbf{r}_{\text{c.g.}}^{E} = \mathbb{T}_{ET}[0 \quad 0 \quad -l_T]^T + \mathbb{T}_{EB}[-x_T \quad 0 \quad -z_T]^T \tag{1}$$

The coordinates $x_T$ and $z_T$ represent the location of the bridle hinge line with respect to the c.g.; thus, to go from the bridle hinge line to the c.g., they must be subtracted. Expressions for the rotation matrices $\mathbb{T}_{ET}$ and $\mathbb{T}_{EB}$ are constructed from the angle definitions in Figs. 2 and 3.

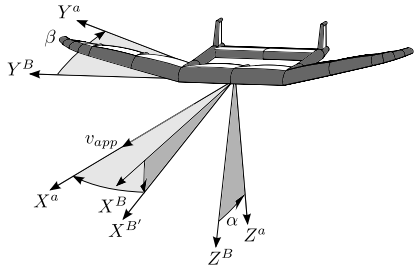


**Fig. 4 Definition of the aerodynamic reference frame.**

The aerodynamic reference frame in Fig. 4 is established from the definition that $X^a$ coincides with the apparent velocity vector of the kite through subsequent rotations $\alpha$ about $Y^B$ and $\beta$ about $Z^a$. The magnitude of the apparent velocity vector $v_{\text{app}}$, the angle of attack $\alpha$, the sideslip angle $\beta$, and the body angular velocity $\boldsymbol{\omega}_{\text{c.g.}}$ together determine the aerodynamic forces and moments on the kite.

### B. Equations of Motion

Lagrange's equation of the second kind, Eq. (2), is used to derive five second-order differential equations that describe the motion of the kite system:

$$\frac{\mathrm{d}}{\mathrm{d}t}\frac{\partial T}{\partial \dot{q}_i} - \frac{\partial T}{\partial q_i} + \frac{\partial V}{\partial q_i} = Q_i, \qquad i = 1, \ldots, 5 \tag{2}$$

The five DOF are represented by the generalized coordinates $q_i$. To evaluate Eq. (2), expressions need to be found for the kinetic energy $T$, the potential energy $V$, and the generalized forces $Q_i$. The kinetic energy is obtained from Eq. (3) by substituting Eq. (4) for $\mathbf{v}_{\text{cg}}$ and Eq. (6) for $\boldsymbol{\omega}_{\text{c.g.}}$:

$$T = \tfrac{1}{2} m_k \mathbf{v}_{\text{c.g.}} \cdot \mathbf{v}_{\text{c.g.}} + \tfrac{1}{2} \boldsymbol{\omega}_{\text{cg}}^T \cdot \mathbb{I} \cdot \boldsymbol{\omega}_{\text{c.g.}} \tag{3}$$

Equation (4) is found by differentiating $\mathbf{r}_{\text{c.g.}}$ with respect to time, and Eqs. (5) and (6) are constructed from the definitions in Sec. II.A:

$$\begin{aligned}\mathbf{v}_{\text{c.g.}}^T = {} & [0 \quad 0 \quad -\dot{l}_T]^T + \boldsymbol{\omega}_{E_T}^T \times [0 \quad 0 \quad -l_T]^T \\ & + \mathbb{T}_{TB} \cdot \boldsymbol{\omega}_{E_B}^B \times [-x_T \quad 0 \quad -z_T]^T\end{aligned} \tag{4}$$

$$\boldsymbol{\omega}_{E_T}^T = \begin{bmatrix} 0 \\ 0 \\ \dot{\chi} \end{bmatrix} + \mathbb{T}_{TE''} \begin{bmatrix} 0 \\ \dot{\phi} \\ 0 \end{bmatrix} + \mathbb{T}_{TE'} \begin{bmatrix} 0 \\ 0 \\ \dot{\psi} \end{bmatrix} \tag{5}$$

$$\boldsymbol{\omega}_{E_B}^B = \begin{bmatrix} 0 \\ \dot{\theta} \\ 0 \end{bmatrix} + \mathbb{T}_{BT} \begin{bmatrix} 0 \\ 0 \\ \dot{\chi} \end{bmatrix} + \mathbb{T}_{BE''} \begin{bmatrix} 0 \\ \dot{\phi} \\ 0 \end{bmatrix} + \mathbb{T}_{BE'} \begin{bmatrix} 0 \\ 0 \\ \dot{\psi} \end{bmatrix} \tag{6}$$

The potential energy is given by Eq. (7), where $m_g$ represents the kite mass excluding the confined air. To avoid inclusion of buoyancy forces, the confined air mass is subtracted from $m_k$, assuming that the centers of mass coincide:

$$V = m_g \mathbf{g} \cdot \mathbf{r}_{\text{c.g.}} \tag{7}$$

Since the kite system is subjected to nonconservative forces such as aerodynamic and ground-station loads, expressions for these forces are required in the form of generalized forces. For a rigid body, the resulting aerodynamic loads can be expressed as a force vector and a moment vector that act on the kite c.g.. In the body reference frame, these two vectors are denoted by, respectively, $\mathbf{F}_a^B$ and $\mathbf{M}_a^B$. The force of the ground station acting on the tether is represented by $\mathbf{F}_{\text{GS}}^T$ in the tether reference frame.

With the nonconservative forces specified, the generalized force $Q_i$ for generalized coordinate $q_i$ can be derived using the principle of virtual work in Eq. (8):

$$Q_i = \frac{\partial \dot{\mathbf{r}}}{\partial \dot{q}_i} \cdot \mathbf{F} + \frac{\partial \dot{\boldsymbol{\omega}}}{\partial \dot{q}_i} \cdot \mathbf{M}, \qquad i = 1, \ldots, 5 \tag{8}$$

The results of applying Eq. (8) to the generalized coordinates in the kite system are displayed in Eqs. (9–13). Note that the nonconservative forces are transformed to the reference frames corresponding to the generalized coordinates:

$$Q_\theta = \frac{\partial}{\partial \dot{\theta}} \left( \mathbf{M}_a^B \cdot \begin{bmatrix} 0 \\ \dot{\theta} \\ 0 \end{bmatrix} + \mathbf{F}_a^B \cdot \left( \begin{bmatrix} 0 \\ \dot{\theta} \\ 0 \end{bmatrix} \times \begin{bmatrix} -x_T \\ 0 \\ -z_T \end{bmatrix} \right) \right) \tag{9}$$

$$Q_\chi = \frac{\partial}{\partial \dot{\chi}} \left( \mathbf{M}_a^T \cdot \begin{bmatrix} 0 \\ 0 \\ \dot{\chi} \end{bmatrix} + \mathbf{F}_a^T \cdot \left( \begin{bmatrix} 0 \\ 0 \\ \dot{\chi} \end{bmatrix} \times \begin{bmatrix} -x_T \\ 0 \\ -z_T \end{bmatrix} \right) \right) \tag{10}$$

$$Q_{l_T} = \frac{\partial}{\partial \dot{l}_T} \left( \left( \mathbf{F}_a^T + \mathbf{F}_{\mathrm{GS}}^T \right) \cdot \begin{bmatrix} 0 \\ 0 \\ -\dot{l}_T \end{bmatrix} \right) \tag{11}$$

$$Q_\phi = \frac{\partial}{\partial \dot{\phi}} \left( \mathbf{M}_a^{E''} \cdot \begin{bmatrix} 0 \\ \dot{\phi} \\ 0 \end{bmatrix} + \mathbf{F}_a^{E''} \cdot \left( \begin{bmatrix} 0 \\ \dot{\phi} \\ 0 \end{bmatrix} \times \mathbf{r}_{\mathrm{c.g.}}^{E''} \right) \right) \tag{12}$$

$$Q_\psi = \frac{\partial}{\partial \dot{\psi}} \left( \mathbf{M}_a^{E'} \cdot \begin{bmatrix} 0 \\ 0 \\ \dot{\psi} \end{bmatrix} + \mathbf{F}_a^{E'} \cdot \left( \begin{bmatrix} 0 \\ 0 \\ \dot{\psi} \end{bmatrix} \times \mathbf{r}_{\mathrm{c.g.}}^{E'} \right) \right) \tag{13}$$

### C. Aerodynamic Model

In the generalized forces, the aerodynamics are incorporated through the force vector $\mathbf{F}_a$ and moment vector $\mathbf{M}_a$. However, an expression for these vectors is yet to be found. For this purpose, strip theory is employed to acquire a parametric model in terms of the geometric properties. The basic idea, illustrated by Fig. 5, is to calculate the aerodynamic forces locally at the aerodynamic elements and then calculate the contribution to $\mathbf{F}_a^B$ and $\mathbf{M}_a^B$ based on the position and orientation of the element in the body reference frame.

An advantage of this approach is that it avoids estimations of stability derivatives, because they are, in fact, accounted for by the relative location and orientation of the aerodynamic elements.

#### 1. Wing Aerodynamics

To incorporate the dihedral angle as a parameter in the model, the wing is split up in two aerodynamic elements: left and right. For the calculation of the lift and drag forces on the wing halves, the airflow is observed at the quarter-chord point of the spanwise location $\bar{y}_w$ of the mean aerodynamic chord (MAC). It is assumed that this point represents the wing half better than the geometric mean that is common in strip theory.

For the calculation of the lift and drag on the wing halves, experimental or theoretical $C_L$–$\alpha$ and $C_D$–$\alpha$ curves can be used to link the local aerodynamic angles to aerodynamic coefficients. In the kiteplane case study, experimental data from [36] is combined with the approach for 3-D plates at an angle from [37] to obtain the curves in Fig. 6.

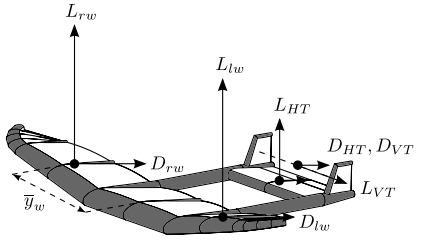


**Fig. 5 Illustration of the aerodynamic element discretization.**

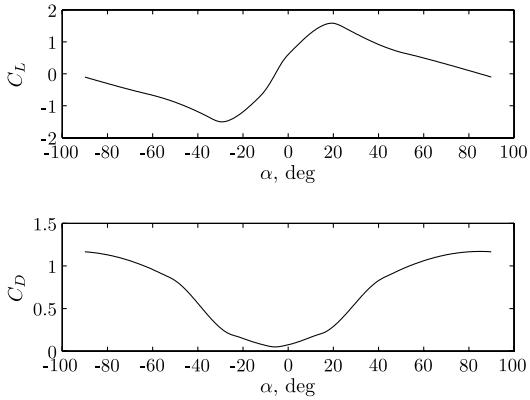


**Fig. 6 $C_L - \alpha$ and $C_D - \alpha$ curves for the kiteplane wing.**

An aspect not covered in strip theory is a nonzero pitching moment of the wing. This can be included separately by using Eq. (14), provided that a value or curve for $C_{m_{\mathrm{ac}}}$ is available:

$$M_{w_{\mathrm{ac}}} = \tfrac{1}{2} \rho \mathbf{v}_a^B \cdot \mathbf{v}_a^B S_w \bar{c}_w C_{m_{\mathrm{ac}}} \tag{14}$$

#### 2. Horizontal Tail Plane Aerodynamics

The contribution of the horizontal tail plane to the aerodynamic forces and moments is calculated essentially in the same way as the contribution of the wing. There are some differences. The local angle of attack needs to be corrected for the downwash of the wing, and the local air velocity is reduced due to the presence of the wing in front. Empirical estimates for these corrections are found using DATCOM [38].

#### 3. Vertical Tail Plane Aerodynamics

As with the other elements, a single resultant force is calculated at the quarter-chord point of the spanwise MAC location. In the kiteplane case study there are, in fact, two vertical fins, which are approximated by a single element using the fins' original MAC locations and aerodynamics properties, but taking into account twice the size. Because of the simplifications in the model, this is equal to including both fins separately when the small effect of the lateral position of the fins on the distance to the equivalent vertical tail plane is neglected. Adapting the model for multiple fin configurations was considered unnecessary at this accuracy level.

### D. Ground-Station Force

Since the tether is modeled as a massless rigid one-dimensional rod, the translational joint between the tether and the ground station accounts for the spring-damper dynamics. This approach combines the tether dynamics and ground-station dynamics in a single force. The ground-station force that represents the spring-damper dynamics of a fixed-length tether is given by Eq. (15), where $k$ represents the spring constant and $d$ is the damping constant. Both properties depend on the tether material, thickness, and length:

$$F_{\mathrm{GS}} = \begin{cases} k(l_T - l_{T0}) + d\dot{l}_T, & l_T \geq l_{T0} \\ 0, & l_T < l_{T0} \end{cases} \tag{15}$$

## III. Results of the Kiteplane Case Study

With the described methodology, analytical and numerical results can be obtained for various aircraft-shaped kites. In this paper a case study is performed on a specific kite, the kiteplane, to investigate whether the developed model can describe its dominating behavior. The kiteplane, displayed in previous figures, features an approximate

**Table 1 Geometric properties of the kiteplane**

| Parameter | Symbol | Value |
|---|---|---|
| Wing | | |
| Surface area | $S_w$ | 5.67 m$^2$ |
| Aspect ratio | $A_w$ | 5.65 |
| Taper ratio | $\lambda$ | 0.66 |
| Dihedral angle[a] | $\Gamma$ | 14 deg |
| MAC | $\bar{c}_w$ | 1.08 m |
| MAC location | $\bar{y}_w$ | 1.21 m |
| Airframe | | |
| Total length | $l$ | 3.08 m |
| Horizontal tail distance | $l_{\mathrm{HT}}$ | 2.24 m |
| Vertical tail distance | $l_{\mathrm{VT}}$ | 2.56 m |
| Horizontal tail | | |
| Surface area | $S_{\mathrm{HT}}$ | 1.28 m$^2$ |
| Aspect ratio | $A_{\mathrm{HT}}$ | 2.2 |
| MAC | $\bar{c}_{\mathrm{HT}}$ | 0.76 m |
| Vertical tail | | |
| 2 × surface area | $S_{\mathrm{VT}}$ | 0.33 m$^2$ |
| Aspect ratio | $A_{\mathrm{VT}}$ | 1.2 |
| Taper ratio | $\lambda_{\mathrm{VT}}$ | 0.59 |
| LE sweep | $\Lambda_{\mathrm{LE,VT}}$ | 23 deg |
| MAC | $\bar{c}_{\mathrm{VT}}$ | 0.38 m |
| MAC location | $\bar{c}_{\mathrm{VT}}$ | 0.20 m |

[a]Of the outer wing.

elliptic wing with positive dihedral from the tail-boom section to the tips and is comparable in size with a small surfkite. The twin tail booms support the horizontal tail plane that is located in-between and the two vertical tail planes on top. The main geometrical properties are listed in Table 1, where the MAC and its location are calculated using the definitions from [39].

The inertia of the kiteplane consists of three parts: the pressurized beam structure, the canopy surfaces, and the air confined in the tubes and airfoils. The contribution of displaced air is assumed to be negligible, because the kiteplane is still about five times heavier than air. Estimations based on the CAD model give the following properties:

$$m_k = 4.21 \text{ kg}, \qquad m_g = 3.44 \text{ kg}$$

$$\mathbf{r}^B_{\mathrm{LE}} = \begin{bmatrix} 0.916 & 0 & 0.089 \end{bmatrix}^T \text{ m}$$

$$\mathbb{I} = \begin{bmatrix} 7.38 & 0 & 0.18 \\ 0 & 4.20 & 0 \\ 0.18 & 0 & 11.43 \end{bmatrix} \text{kgm}^2$$

The vector $\mathbf{r}^B_{\mathrm{LE}}$ represents the position of the leading edge (LE) with respect to the c.g. in the body reference frame. Apparently, the center of gravity is located at about 92 cm behind the leading edge of the wing, which is at approximately 85% of the MAC.

### A. Analytical Stability Analysis

By examining the free-body diagram of the kite, the static stability of distinct motions of the system can be determined. However, when the kite is located in the plane spanned by the wind velocity $v_W$ and the vertical, the symmetry plane, the results are equivalent to that of a regular airplane. The only difference, the tether force, acts in this case as additional gravity and thrust. This situation can be viewed as gliding flight.

Application of airplane stability analysis (as described by, for example, [40–42]) to the kiteplane yields longitudinal static stability in the symmetry plane if $v_W > 3$ m/s, depending on the angle of attack. Although the aerodynamic center (ac) of the kiteplane is located at approximately $l_{\mathrm{HT}}(S_{\mathrm{HT}}/S) = 0.51$ m behind the wing ac, or 15 cm in front of the c.g., the tether force moves the apparent c.g. in front of the aerodynamic center if the lift exceeds the weight. The results of the longitudinal stability analysis are summarized in Fig. 7, which shows the pitch- and zenith-angle equilibrium in $\phi$–$\alpha$ space. The arrows give an indication of the convergence.

The angle of attack that satisfies pitch equilibrium does not depend on $\phi$ and is therefore a horizontal straight line. The equilibrium in zenith angle is more interesting, because it is equivalent to the $L/D$, including weight effects, for a specific angle of attack and wind velocity. The maximum $L/D$, or minimal equilibrium $\phi$, is achieved at $\alpha \approx 8$ deg. However, these equilibrium lines will shift if the operating conditions change. For example, a higher wind velocity reduces the relative effect of gravity, and this will cause the solid line to shift to the left for a higher $L/D$ and cause the dashed line to shift downward for a lower lift coefficient.

Lateral stability analysis in the symmetry plane, without lateral components of the tether force and gravity, shows that the kiteplane is statically stable in pure roll (low elevation) and pure yaw (high elevation). Because positive rotation about $X^B$ initiates positive rotation about $Z^B$ and vice versa, rotation about $Z^T$ is a statically stable combination of the investigated extremes. Furthermore, sideslipping is dynamically stable.

If the kite moves outside the symmetry plane, the situation is fundamentally different from airplane motion, due to the constraints posed by the fixed-length tether and the bridle connection. In this condition, the tether force and gravity start to interfere in the roll and yaw motions of the kite. To investigate the stability of this motion, the reduced model displayed in Fig. 8, with the two DOF $\theta_T$ and $\chi$, is analyzed.

Pendulum stability requires the kiteplane to converge to the situation displayed in Fig. 8 from a disturbance in $\theta_T$. To investigate the pendulum stability, the situation in Fig. 9 is considered. This is a typical scenario in which, for the observer, the kiteplane is located on the left side and falling to the left side. It is assumed that $\chi$ changes such that the kiteplane always points approximately into the wind ($-X^E$), because then the lateral force $F^B_Y$ is tangential to the pendulum arc and relates directly to $\theta_T$. This assumption restrains the DOF $\chi$,

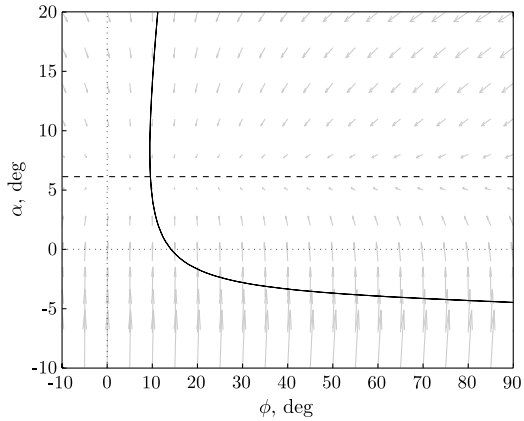


**Fig. 7 Static longitudinal stability with zenith equilibrium (solid line) and pitch equilibrium (dashed line).**

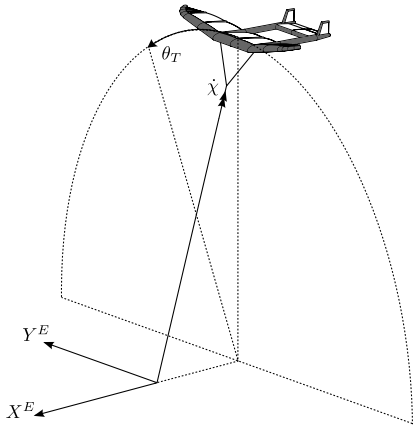


**Fig. 8 Kiteplane system pendulum motion.**

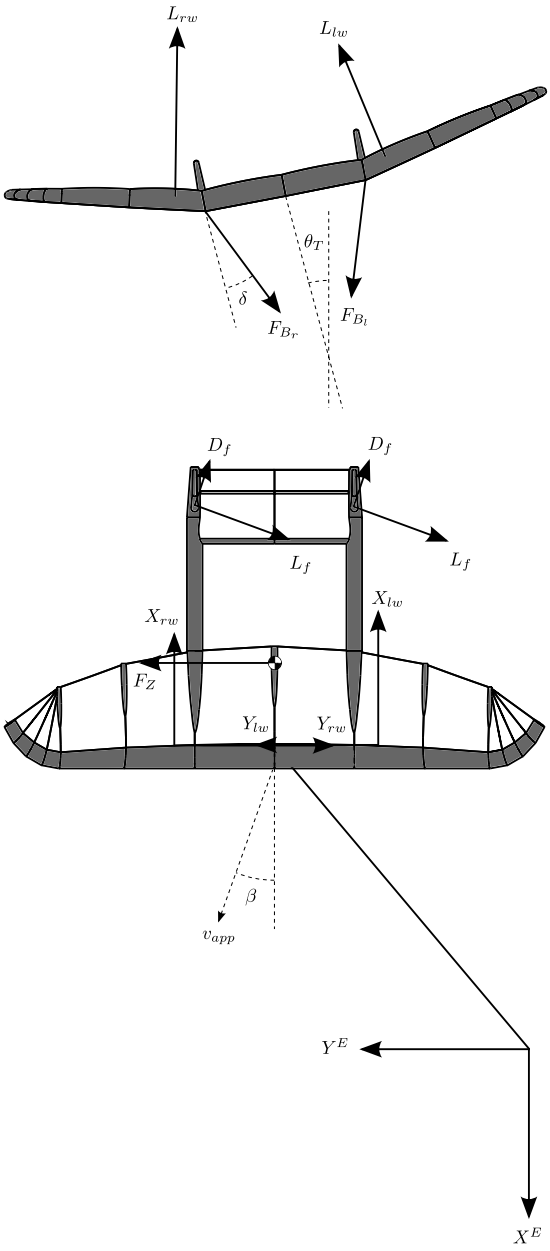


**Fig. 9 Front and top view of the kiteplane in pendulum motion.**

but aerodynamically the rotation about $Z^T$ is governed by $\beta$, which is free and replaces $\chi$ as the second DOF.

To find quantitative results for the pendulum stability, the following case constants are introduced:

$$\rho = 1.225\ \text{kgm}^{-3}, \qquad g = 9.81\ \text{ms}^{-2}$$
$$x_T = 0.65\ \text{m}, \qquad \frac{v_t}{v} = 0.95$$
$$z_T = 0.2\ \text{m}, \qquad v_W = 6\ \text{m/s}$$
$$\alpha = 5\ \text{deg}, \qquad \theta = -5\ \text{deg}$$

Because the pendulum motion is a combination of $\theta_T$ and $\beta$, strictly necessary conditions for static stability are difficult to define; however, four sufficient conditions can be formulated using Eq. (16):

$$\mathrm{d}F_Y^B/\mathrm{d}\theta_T < 0, \qquad \mathrm{d}F_Y^B/\mathrm{d}\beta < 0$$
$$\mathrm{d}M_Z^T/\mathrm{d}\theta_T < 0, \qquad \mathrm{d}M_Z^T/\mathrm{d}\beta > 0$$

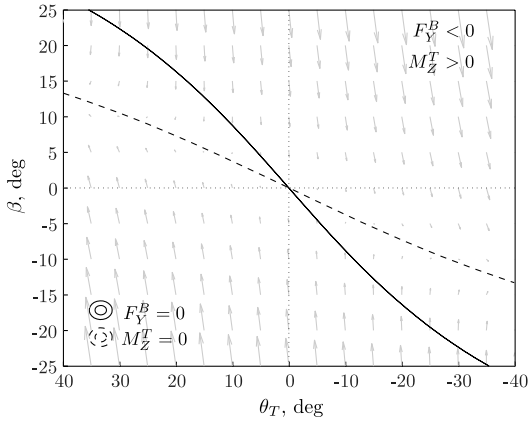


**Fig. 10 Pendulum stability with $\theta_T$ equilibrium (solid line) and $\beta$ equilibrium (dashed line).**

$$M_Z^T = M_Z^B \cos(\theta) + M_X^B \sin(-\theta) \tag{16}$$

With the case constants substituted, $F_Y^B$ and $M_Z^T$ can be plotted as functions of $\theta_T$ and $\beta$. Figure 10 displays the lines $F_Y^B = 0$ and $M_Z^T = 0$ in $\theta_T$–$\beta$ space. The lines represent the equilibrium condition for $Y^B$ and $Z^T$. The only equilibrium for the pendulum motion is found at the point (0,0) in Fig. 10, which is the trivial equilibrium in the symmetric plane. The arrows indicate in which direction the kiteplane is accelerated. In steady state, they are a measure for the acceleration vector in $\theta_T$–$\beta$ space with $x$ component $\ddot{\theta}_T$ and $y$ component $\ddot{\beta}$.

Observation of the gradients yields the conclusion that three out of four of the sufficient conditions for static pendulum stability are met. The derivative $\mathrm{d}F_Y^B/\mathrm{d}\theta_T$ is positive instead of negative, as it would be required for stability.

Nonetheless, if a positive equilibrium $\beta$ results in a negative value for $F_Y^B$, the system may still be stable. This means that in Fig. 10 the dashed $M_Z^T$ line should be steeper than the solid $F_Y^B$ line, but this is not the case. Similar conclusions can be drawn from following the arrows in Fig. 10, which results in diverging either to the left or to the right.

The analysis in this section proves that the kiteplane system restricted to pendulum motion is unstable. This cannot be guaranteed for the unrestricted kiteplane system, but it is nevertheless likely that it exhibits some of this unstable behavior. The investigation of this pendulum motion is continued trough numerical simulation.

### B. Numerical Simulation Results

To study the motion of the kiteplane, numerical simulations are produced with a MATLAB/Simulink model that is constructed from the derived equations of motion. The model is used to solve initial value problems, for which the results can subsequently be compared with other simulations or flight tests.

#### *1. Flight-Test Comparison*

To test the validity of the model, a typical test flight is reconstructed. The state of the kiteplane after the launch is estimated from flight-test footage and fed into the model as initial conditions. The simulated motion and estimated initial conditions are displayed in Fig. 11. The corresponding flight-test footage is shown in Fig. 12 for comparison. The 3-D flight path displayed in Fig. 11 is similar to that in Fig. 12, but the motion takes 40% more time in the simulation. This is a significant difference, but both seem to show the same instability.

Because of the initial sideslip angle, the kiteplane starts moving in the $-Y^E$ direction and rotating about the $Z^T$ axis. At 4 s, the kiteplane reaches its maximum $\psi$ angle and slowly starts moving in $Y^E$ direction. Because of the high inertia in $Y^E$ motion compared with the inertia in $Z^T$ rotation, the kiteplane is already highly rotated before the motion in $Y^E$ direction gains momentum. This behavior causes the kiteplane to reach a sideslip angle of almost $-40$ deg at $t = 6$ s.

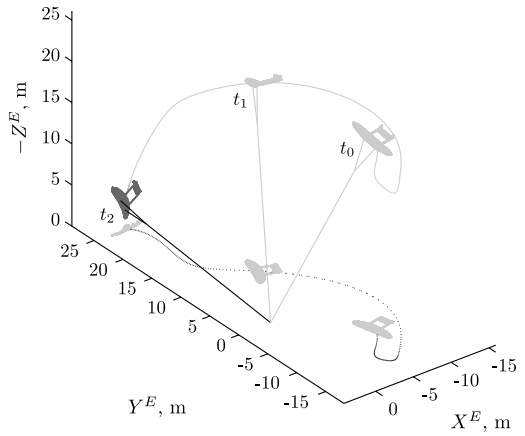


**Fig. 11 3-D path of diverging motion with asymmetric and static initial conditions: $\theta = -10$ deg, $\chi = -60$ deg, $l_T = 25$ m, $\phi = 25$ deg, $\psi = 45$ deg, and $\Delta t = 17$ s.**

**Fig. 12 Composite photo constructed from flight-test footage with $v_W \approx 6$ m/s, the flight time captured in this figure is approximately 12 s.**

From this point on, the kiteplane starts accelerating in the $Y^E$ direction, with increasing $\alpha$, increasing $v_{\text{app}}$, and quickly reducing $\beta$. At the passing of $-X^E$, the same inertia that initially kept the kiteplane from returning to $\psi = 0$ is now causing a major overshoot in $\psi$. At about 11 s, the kiteplane is pushed toward a point of no return and falls to the ground. The increase in $\beta$ at this point is insufficient to generate a large-enough aerodynamic force in the $-Y^B$ direction to overcome the gravity component in the $Y^B$ direction.

The pendulum motion that was studied analytically in the previous section seems dominant in this flight, and it appears that the analytical approach and the simulation agree on the instability that is observed in reality. A comparison of the simulation and the analytical pendulum analysis is displayed in Fig. 13. The simulated trajectory in $\theta_T$–$\beta$ space is indicated by the gray line, with the circle marking the starting point and the cross marking the final state.

Thus, in the starting condition, $F_Y^B$ is negative and $M_Z^T$ is positive. This is in correspondence with the motion displayed in Fig. 11. Subsequently, this motion causes the kiteplane to move to another position in $\theta_T$–$\beta$ space, where $F_Y^B$ is positive and $M_Z^T$ is negative. This, in turn, causes the kiteplane to move in the direction of $Y^E$ with increasing velocity. This increase in velocity reduces the inertia effects, compared with the aerodynamic effects, and the gray line starts to converge toward the dashed black line in the upper right quadrant. However, the equilibrium sideslip angle never results in a sufficiently large sideslip angle for $\theta_T$ to convergence. While the sideslip angle is slowly converging, the kiteplane is falling to the side.

From the acceleration arrows alone, one would expect the kiteplane to fall to the right side by converging to the dashed black line on the right. At first, the gray line seems to do exactly that, but at a certain point the line shoots downward in the area that pushes the

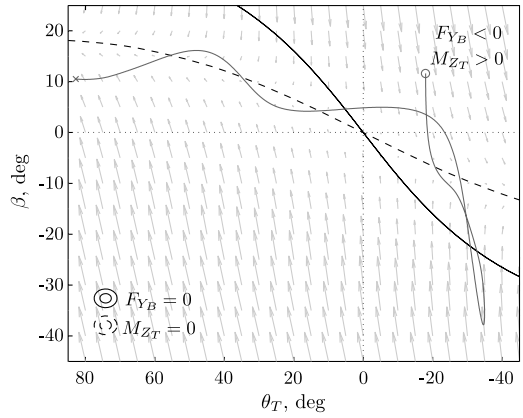


**Fig. 13 Pendulum static stability applied to diverging motion (solid line) with asymmetric and static initial conditions: $\theta = -10$ deg, $\chi = -60$ deg, $l_T = 25$ m, $\phi = 25$ deg, $\psi = 45$ deg, and $\Delta t = 17$ s.**

kiteplane back to the middle. Apparently, not all important effects are described by the static 2-DOF approximation. This could be expected, because the assumptions that the apparent wind velocity is equal to the wind velocity, that the heading coincides roughly with $X^E$, that the body rotational velocities are small, and that the roll-yaw coupling is constant do not hold throughout this flight trajectory.

Moreover, it appears that, in reality, the asymmetric motion is more stable than Fig. 13 suggests. Because of the inertia in rotation about the tether, the sideslip convergence can be either periodic or aperiodic. If the sideslip motion is periodically converging, the overshoot that causes the heading of the kiteplane to point toward the middle triggers the symmetric motion. This leads to mixing of the unstable asymmetric motion with the stable symmetric motion, which increases the apparent lateral stability.

If the dashed line in Fig. 13 is relatively steep, i.e., sideslip equilibrium is achieved at high sideslip angles, the kiteplane tends to rotate more, and this induces the mixing of symmetric and asymmetric motion. A relatively flat solid line, which it is not in this case, allows more time for rotation and hence increases apparent lateral stability. In fact, the kiteplane system can be stable even when the solid line is slightly steeper than the dashed line.

To summarize, the validity of the static 2-DOF analysis is limited, but it does provide useful insights into the cause of the instability. It seems essential to have a small-enough vertical tail plane to achieve a large-enough equilibrium sideslip angle and to have a large-enough lateral area to generate a strong-enough lateral force. To test this hypothesis, simulations are run with various vertical tail plane sizes and dihedral angles.

### 2. *Impact of Design Variations on Stability*

Inspection of Table 1 yields many geometrical parameters to investigate, but only those with the largest impact on the stability are really interesting for the scope of this paper. The main parameters for longitudinal stability are $S_{\text{HT}}/S_w$ and $l_{\text{HT}}/\bar{c}$. Since this case study is on the kiteplane, the wing dimensions are kept constant for convenience, and varying $S_{\text{HT}}$ and $l_{\text{HT}}$ is therefore equivalent to varying the ratios.

Figure 14 shows the effect of reducing the tail-boom length on longitudinal stability. The trajectory indicated by the gray lines is the launch motion, and the dashed line represents that for the original size. The effect of reducing $S_{\text{HT}}$ by 20% yields similar results. Apparently, the horizontal tail plane contribution can be reduced without jeopardizing stability; the 20% reduction even decreases the overshoot in $\phi$ significantly.

For the lateral stability, the interesting parameters are $S_{\text{VT}}$, $l_{\text{VT}}$, and $\Gamma$. Next to these parameters, the inclusion of an additional lateral surface on top or below the wing is also regarded as interesting. The main effect of such a surface can also be achieved with dihedral, but secondary effects are inherently different. The most noticeable

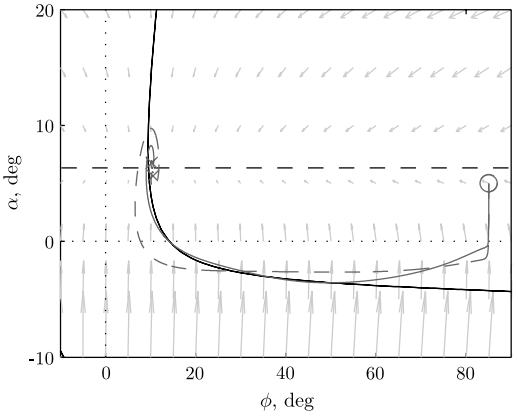


**Fig. 14 Effect of 20% reduction in tail-boom length on longitudinal stability during launch, original length (dashed line) and reduced length (solid line).**

difference is the effect of dihedral on the yaw moment, which is absent for a single vertical surface in the middle of the kiteplane.

Nevertheless, the parameters $S_{\mathrm{VT}}$ and $\Gamma$ are selected for the lateral stability investigation. Keeping the tail-boom length constant avoids side effects on longitudinal stability, and adjusting $\Gamma$ is simply found to be more elegant than the addition of a vertical surface. The impact of variations in $S_{\mathrm{VT}}$ and $\Gamma$ on the inertia is neglected to keep the results, depending on geometry only. The effects due to changing inertia will be investigated at a later stage.

The stability is assessed based on simulation results in the range of $-10\,\mathrm{deg} < \Gamma < 40\,\mathrm{deg}$ and $0 < (S_{\mathrm{VT}}/S_{\mathrm{VT0}}) < 8$ for two different wind velocities. The arrangements of the stability domains are displayed in Fig. 15. Basically, small vertical tail planes cause diverging oscillations, and low dihedral angles cause aperiodic divergence. Stability requires a large dihedral angle and a vertical tail plane of about one to three times the original size. Furthermore, the stable domain increases with increasing wind velocity.

For low dihedral angles and low wind velocities, increasing the vertical tail size leads from unstable oscillations to aperiodic divergence. If the dihedral angle and wind velocity are large enough, a stable regime emerges in-between. The stable regime itself consists of three domains. The first, for a small vertical tail plane, is the stable oscillation. The second, for a medium-sized vertical tail plane, is the converging oscillation. For large vertical tail planes and low dihedral angles, a domain of aperiodic convergence exists. For higher wind velocities, the aperiodic-convergence domain increases in size at the cost of the converging-oscillation domain.

At the boundary of diverging oscillation and stable oscillation something peculiar occurs, which is visible in Figs. 15a and 15b. At a vertical tail plane size slightly too small for stable oscillation, there seems to be a small band of $\Gamma$ values that still yield a semistable oscillation. When the vertical tail plane area is reduced sightly from stable oscillation, the stable figure-eight pattern starts to oscillate itself. This behavior can be compared with the precession of the rotation axis of a spinning top. For most cases, the crossing of the figure eight starts to move in the $Y^E$ direction, one circle becomes larger than the other, and the kiteplane eventually crashes into the ground.

Another feature that is invisible in Figs. 15c and 15d are the roots of the different stable domains. These figures reveal that there is always a converging-oscillation domain below the stable-oscillation domain and that the arrangement of the aperiodic-convergence domain depends greatly on wind velocity.

The pendulum stability according to the five stability domains with a sample flight trajectory are displayed in Fig. 16. The equilibrium lines in Fig. 16 are calibrated to the average conditions during the trajectory.

The first thing to note is that the differences between the equilibrium lines are small, compared with the resulting trajectory. Although the behavior and geometry in both unstable domains is

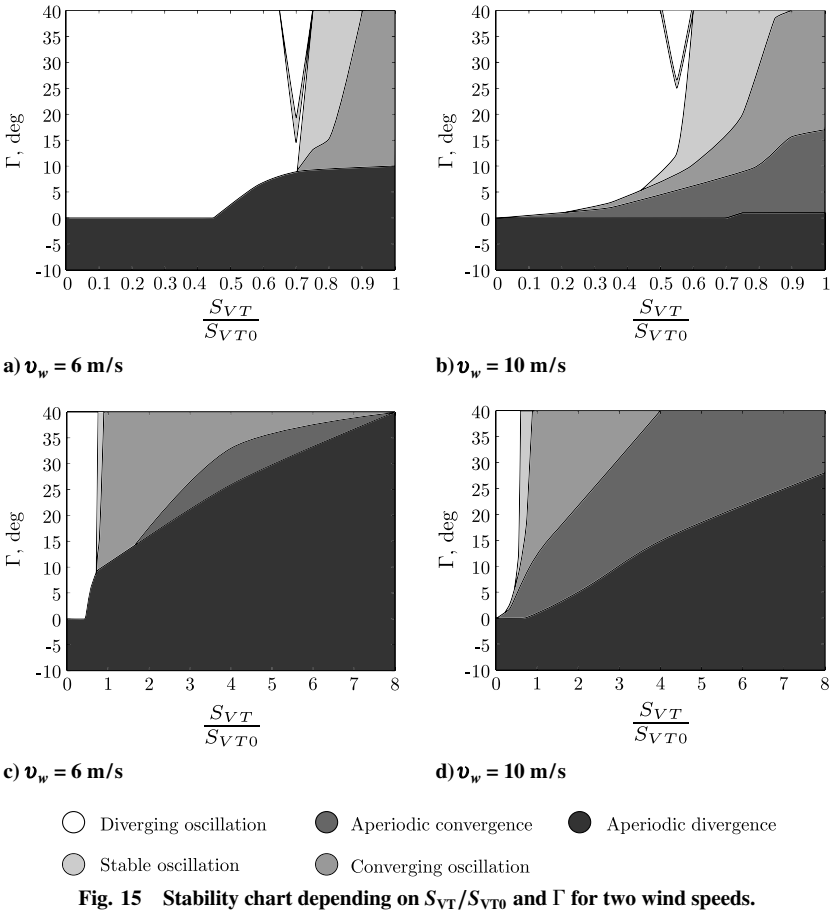


**Fig. 15 Stability chart depending on $S_{\mathrm{VT}}/S_{\mathrm{VT0}}$ and $\Gamma$ for two wind speeds.**

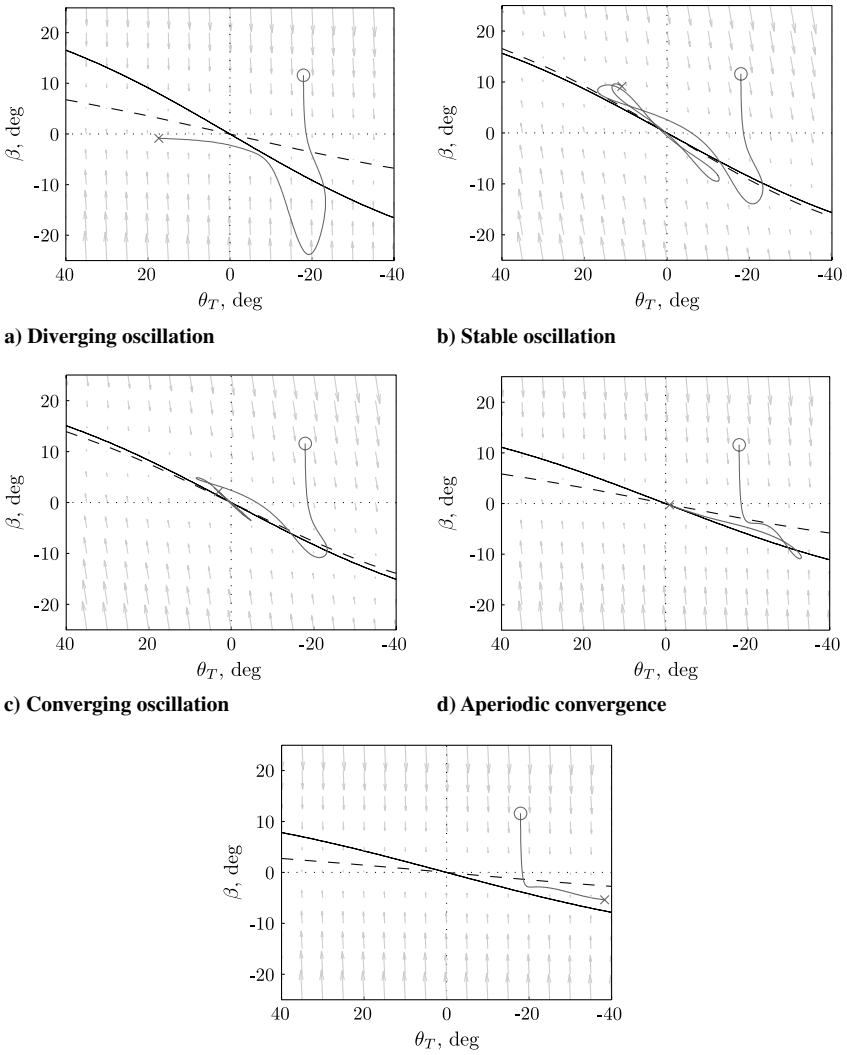


**Fig. 16 Pendulum stability with $\theta_T$ equilibrium (solid line) and $\beta$ equilibrium (dashed line) according to the five different stability domains, including sample trajectories starting at the circle mark.**

significantly different, the equilibrium lines have a similar slope difference. It appears that, in general, if the difference between the slopes of the solid and dashed lines become too large, then the system becomes unstable.

The stable-oscillation domain displayed in Fig. 16b is the desired stability space according to the pendulum stability analysis in Sec. III.A. The dashed line is steeper than the solid line, which means that the kiteplane converges to a sideslip angle that generates a resultant force toward $\theta_T = 0$. However, the lack of damping of this configuration results in continued oscillations.

At the border of stable oscillation and converging oscillation, the dashed line is on top of the solid line. From the 2-DOF pendulum-motion point of view, this is the border to unstable behavior. However, the longitudinal stability improves lateral stability and is, in fact, crucial in the entire converging domain.

If the solid line is only slightly steeper than the dashed line, the motion is still oscillatory. If the difference in slope becomes larger, the oscillations disappear. This is the domain of aperiodic convergence and illustrates the improved apparent lateral stability very clearly, because the acceleration arrows indicate divergence.

Nevertheless, if the lateral instability becomes too large for the longitudinal stabilization, the motion diverges, as displayed in Fig. 16e. The absolute slope differences in Figs. 16d and 16e are about equal, but the relative difference is larger, because the slopes in Fig. 16e are shallower.

As an additional illustration of the motion of the kiteplane system, a sample trajectory of stable oscillation is displayed in Fig. 17. The trajectory starts with a launch from a slightly asymmetric initial condition: $\chi = -10\,\text{deg}$ and $\psi = 10\,\text{deg}$.

### 3. *Impact of Operating Conditions on Stability*

During kite flight, various operational conditions occur. Also, the presented model is a simplification of reality based on assumptions that have an impact on accuracy. For these reasons, it is important that

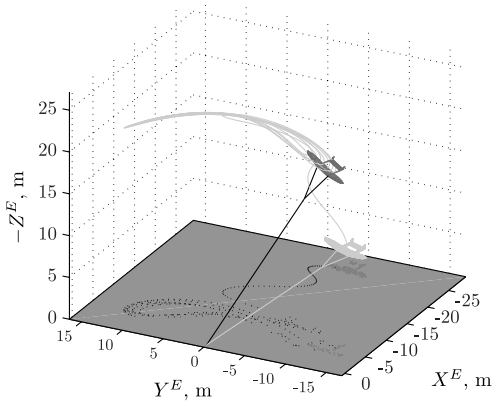


**Fig. 17 Stable-oscillation trajectory for $\Gamma = 20\,\text{deg}$, $S_{VT}/S_{VT0} = 0.63$ and $v_W = 10\ \text{ms}^{-1}$.**

**Table 2 Impact of operating conditions on stability**

| Variation | Asymmetric initial conditions | Lateral step gust of 0.5 $v_W$ |
|---|---|---|
| | *Reference* | |
| —— | Converging oscillation | Converging oscillation |
| | *Inertia* | |
| −30% | More damped oscillation | More damped oscillation |
| +30% | Less damped oscillation | Less damped oscillation |
| | $\Gamma$ | |
| −30% | Aperiodic convergence | Aperiodic convergence |
| +30% | Less damped oscillation | Less damped oscillation |
| | $S_{VT}/S_{VT0}$ | |
| −30% | Less damped oscillation | Less damped oscillation |
| +30% | More damped oscillation | More damped oscillation |
| | $x_T$ | |
| 0.0 m | More damped oscillation | More damped oscillation[a] |
| 0.55 m | Aperiodic convergence | Aperiodic convergence |
| 0.6 m | Aperiodic divergence | Aperiodic divergence |
| | $l_T$ | |
| 10 m | More damped oscillation | More damped oscillation |
| 100 m | Equal damping, longer period | Equal damping, longer period, and lower amplitude |
| | $v_W$ | |
| 4 $ms^{-1}$ | Less damped oscillation[a] | Less damped oscillation[a] |
| 16 $ms^{-1}$ | More damped oscillation[a] | More damped oscillation[a] |

[a]Requires new trim setting for proper longitudinal equilibrium in $\alpha$

stability holds for both varying conditions and small design variations. To determine the impact of these variations on stability, several simulations are run, where each simulation varies a single parameter. The results of these simulations are compared with the converging-oscillation reference case with the following parameter values:

$$v_W = 8 \text{ m/s}, \qquad \Gamma = 20 \text{ deg}, \qquad l_T = 25 \text{ m}$$
$$S_{VT}/S_{VT0} = 1.5, \qquad x_T = 0.3 \text{ m}$$

All other parameters are equal to the original design values. The simulation results are summarized in Table 2.

According to the results in Table 2, the stability of the reference case seems robust. To find out if the robustness holds for combined variations, the following two cases are assessed:

1) Inertia +30%, $\Gamma$ +30%, and $S_{VT}/S_{VT0}$ −30%.

2) Inertia −30%, $\Gamma$ +30%, and $S_{VT}/S_{VT0}$ +30%.

The first case (which leans toward diverging oscillations) and the second case (which leans toward aperiodic divergence) are, in fact, still converging. Although the latter is on the verge of aperiodic divergence, these results are promoting the idea of a configuration that is stable in the entire operating domain.

## IV. Conclusions

The geometric requirements for stable flight dynamics of a kiteplane are different from those of regular airplanes. Similarities are found in the longitudinal motion, but the constraints resulting from the tether and the bridle connection give rise to instabilities in the lateral motion outside the symmetry plane. The pendulum motion, in particular, poses additional requirements for stability.

With the developed rigid-body model, an explanation is found for the pendulum instability of the kiteplane design considered in the case study. The analytical analysis yields the hypothesis that a large wing dihedral angle combined with a small vertical tail plane area provides pendulum stability. The small vertical tail plane causes the equilibrium sideslip angle to be large enough for the effective lateral area to generate an aerodynamic force that opposes and overcomes the lateral component of gravity.

Numerical simulations of the derived equations of motion confirm the hypothesis, but the criteria on the geometry appear to be less strict. Because of the mixing of longitudinal and lateral motions, stability is achieved with a larger vertical tail plane area than that predicted by the analytical results. In addition, it is found that reducing the horizontal tail plane area by 25% improves the convergence of the longitudinal motion.

The numerical simulations are only partially successful in reconstructing the presented test flight, but this may be improved when more and accurate data become available for calibration of the model.

The results indicate that the stability of the kiteplane is highly dependent on lateral area parameters. More precisely, the simulation results show that the 2-D kiteplane design space spanned by dihedral angle and vertical tail plane area consists of the five different stability domains:

1) A dihedral angle >5 deg and a vertical tail <3% wing area yields unstable oscillation.

2) A dihedral angle ∼25 deg and a vertical tail ∼4.5% wing area yields stable oscillation.

3) A dihedral angle ∼25 deg and a vertical tail ∼9% wing area yields converging oscillation.

4) A dihedral angle ∼25 deg and a vertical tail ∼25% wing area yields aperiodic convergence.

5) A dihedral angle <10 deg and a vertical tail >25% wing area yields aperiodic divergence.

In respect to these stability domains, the investigated kiteplane design features a too-small lateral area that is distributed too far to the back. A geometry change that moves the design to the converging-oscillation domain is, according to the simulation results, stable for a solid range in design inaccuracies and operational conditions.

## Acknowledgments

The authors are grateful for the financial support provided by the Rotterdam Climate Initiative and the province of Friesland. They appreciate the cooperation of Lam Sails, Ltd., in the production and the engagement of R. Verheul of the Institute for Applied Sustainable Science Engineering and Technology of Delft University of Technology in the design, construction, and testing of the kiteplane prototype.

## References

[1] Breukels, J., and Ockels, W. J., "Past, Present and Future of Kites and Energy Generation," *Power and Energy Systems Conference 2007*, Clearwater, FL, 3–5 Jan. 2007.

[2] Archer, C., and Caldeira, K., "Global Assessment of High-Altitude Wind Power," *Energies*, Vol. 2, No. 2, 2009, pp. 307–319. doi:10.3390/en20200307

[3] Barthel, F., Cabrera, M., Faaij, A., Giroux, M., Hall, D., Kagramanian, V., et al., "Energy Resources," *World Energy Assessment: Energy and the Challenge of Sustainability*, United Nations Development Programme, New York, 2000, Chap. 5.

[4] Loyd, L., "Crosswind Kite Power," *Journal of Energy*, Vol. 4, No. 3, 1980, pp. 106–111. doi:10.2514/3.48021

[5] Ockels, W. J., "Wind Energy Converter Using Kites," European Patent EP084480, Dutch Patent NL1004508, Spanish Patent SP2175268, U.S. Patent US6072245, filed Nov. 1996.

[6] Ockels, W. J., "Laddermill, a Novel Concept to Exploit the Energy in The Airspace," *Aircraft Design*, Vol. 4, 2001, pp. 81–97. doi:10.1016/S1369-8869(01)00002-7

[7] Harvey, M., "The Quest to Find Alternative Sources of Renewable Energy is Taking to the Skies," *The Times*, 12 Nov. 2009, http://business.timesonline.co.uk/tol/business/industry_sectors/utilities/article6913119.ece [retrieved 19 May 2010].

[8] Vance, E., "Wind Power: High Hopes," *Nature*, Vol. 460, 2009, pp. 564–566. doi:10.1038/460564a

[9] Canale, M., Fagiano, L., and Milanese, M., "KiteGen: A Revolution in Wind Energy Generation," *Energy*, Vol. 34, 2009, pp. 355–361. doi:10.1016/j.energy.2008.10.003

[10] Lansdorp, B., and Ockels, W. J., "Comparison of Concepts for High-Altitude Wind Energy Generation with Ground Based Generator," *2nd China International Renewable Energy Equipment & Technology Exhibition and Conference*, Beijing, 25–27 May 2005.

[11] Lansdorp, B., and Ockels, W. J., "Design of a 100 MW Laddermill for Wind Energy Generation from 5 km Altitude," *7th World Congress on Recovery, Recycling and Reintegration*, Beijing, 25–29 Sept. 2005.

[12] Bryant, L. W., Brown, W. S., and Sweeting, N. E., "Collected Researches on the Stability of Kites and Towed Gliders," Aeronautical Research Council, TR 2303, London, 1942.
[13] Etkin, B., "Stability of a Towed Body," *Journal of Aircraft*, Vol. 35, No. 2, 1998, pp. 197–205. doi:10.2514/2.2308
[14] Lambert, C., and Nahon, M., "Stability Analysis of a Tethered Aerostat," *Journal of Aircraft*, Vol. 40, No. 4, 2003, pp. 705–715. doi:10.2514/2.3149
[15] Breukels, J., "KitEye," *Faculty of Aerospace Engineering*, Delft Univ. of Technology, Delft, The Netherlands, 2005.
[16] Breukels, J., and Ockels, W. J., "Design of a Large Inflatable Kiteplane," 48th AIAA/ASME/ASCE/AHS/AHC Structures, Structural Dynamics, and Materials Conference, AIAA Paper 2007-2246, Honolulu, April 2007.
[17] Breukels, J., and Ockels, W. J., "Tethered 'Kiteplane' Design for the Laddermill Project," *4th World Wind Energy Conference & Renewable Energy Exhibition 2005*, Melbourne, Australia, 2–5 Nov. 2005.
[18] Glauert, M., "The Stability of a Body Towed by a Light Wire," Aeronautical Research Council, TR 1312, London, 1930.
[19] Jackson, S., "Free-Flight Tests on Kites in the 24 ft. Wind Tunnel," Aeronautical Research Council, TR 2599, London, 1942.
[20] Sanchez, G., "Dynamics and Control of Single-Line Kites," *The Aeronautical Journal*, Vol. 110, No. 1111, 2006, pp. 615–621.
[21] Alexander, K., and Stevenson, J., "Kite Equilibrium and Bridle Length," *The Aeronautical Journal*, Vol. 105, No. 1051, 2001, pp. 535–541.
[22] Jackson, P., "Optimal Loading of a Tension Kite," *AIAA Journal*, Vol. 43, No. 11, 2005, pp. 2273–2278. doi:10.2514/1.3543
[23] Williams, P., Lansdorp, B., Ruiterkamp, R., and Ockels, W. J., "Modeling, Simulation, and Testing of Surf Kites for Power Generation," AIAA Modeling and Simulation Technologies Conference and Exhibit, AIAA Paper 2008-6693, Honolulu, 18–21 Aug. 2008.
[24] Williams, P., Lansdorp, B., and Ockels, W. J., "Optimal Crosswind Towing and Power Generation with Tethered Kites," *Journal of Guidance, Control, and Dynamics*, Vol. 31, No. 1, 2008, pp. 81–93. doi:10.2514/1.30089
[25] Fagiano, L., "Control of Tethered Airfoils for High-Altitude Wind Energy Generation," Ph.D. Dissertation, Royal Turin Polytechnic, Turin, Italy, 2009.
[26] Houska, B., and Diehl, M., "Optimal Control of Towing Kites," *Proceedings of the 45th IEEE Conference on Decision & Control*, Inst. of Electrical and Electronics Engineers, Piscataway, NJ, 13–15 Dec. 2006. doi:10.1109/CDC.2006.377210
[27] Dadd, G. M., Hudson, D. A., and Shenoi, R. A., "Comparison of Two Kite Force Models with Experiment," *Journal of Aircraft*, Vol. 47, No. 1, 2010, pp. 212–224. doi:10.2514/1.44738
[28] Meijaard, J. P., Ockels, W. J., and Schwab, A. L., "Modelling of the Dynamic Behaviour of a Laddermill, A Novel Concept to Exploit Wind Energy," *Proceedings of the 3rd International Symposium on Cable Dynamics*, Trondheim, Norway, 16–18 Aug. 1999, pp. 229–234.
[29] DeLaurier, J. D., "An Aerodynamic Model for Flapping-Wing Flight," *The Aeronautical Journal*, Vol. 97, No. 964, 1993, pp. 125–130.
[30] Kim, D.-K., Lee, J.-S., Lee, J.-Y., and Han, J.-H., "An Aeroelastic Analysis of a Flexible Flapping Wing Using Modified Strip Theory," *Proceedings of SPIE: The International Society for Optical Engineering*, Vol. 6928, 2008, Paper 69281O. doi:10.1117/12.776137.
[31] Zatzkis, H., "Classical Mechanics," *Fundamental Formulas of Physics*, 2nd ed., Vol. 1, Courier Dover, NewYork, 1960, Chap. 5, Sec. 1.4.
[32] Williams, P., Lansdorp, B., and Ockels, W. J., "Optimal Trajectories for Tethered Kite Mounted on a Vertical Axis Generator," *AIAA Modeling and Simulation Technologies Conference and Exhibit*, AIAA Paper 2007-6706, Hilton Head, SC, 20–23 Aug. 2007.
[33] Williams, P., Lansdorp, B., and Ockels, W. J., "Modeling of Optimal Power Generation Using Multiple Kites," AIAA Modeling and Simulation Technologies Conference and Exhibit, AIAA Paper 2008-6691, Honolulu, HI, 18–21 Aug. 2008.
[34] Williams, P., Lansdorp, B., and Ockels, W. J., "Flexible Tethered Kite with Moveable Attachment Points, Part I: Dynamics and Control," AIAA Atmospheric Flight Mechanics Conference and Exhibit, AIAA Paper 2007-6628, Hilton Head, SC, 20–23 Aug. 2007.
[35] Breukels, J., and Ockels, W. J., "A Multi-Body Dynamics Approach to a Cable Simulation for Kites," *Asian Modelling and Simulation Conference*, Beijing, 8–10 Oct. 2007.
[36] Fink, M. P., "Full-Scale Investigation of the Aerodynamic Characteristics of a Sailwing of Aspect Ratio 5.9," NASA Langley Research Center TN D-5047, Hampton, VA, 1969.
[37] Hoerner, S. F., *Fluid-Dynamic Drag*, Hoerner Fluid Dynamics, Vancouver, Canada, 1965.
[38] Hoak, D. E., and Finck, R. D., "The USAF Stability and Control DATCOM," U.S. Air Force Wright Aeronautical Labs., TR 83-3048, Wright-Patterson AFB, OH, 1960, Sec. 4.4.1.
[39] Torenbeek, E., *Synthesis of Subsonic Airplane Design*, Delft Univ. Press, Delft, The Netherlands, 1982, Appendix A-3.3.
[40] Etkin, B., *Dynamics of Atmospheric Flight*, Wiley, New York, 1972.
[41] Roskam, J., *Airplane Flight Dynamics and Automatic Flight Controls*, DARcorporation, Lawrence, KS, 2001.
[42] Mulder, J. A., van Staveren, W. H. J. J., van der Vaart, J. C., and de Weerdt, E., *Flight Dynamics*, Delft Univ. of Technology, Delft, The Netherlands, 2006.